Supporting Information

Hierarchical dual-protection design in anti-chloride GO/Co_3O_4/$Co_xTi_4O_9$/TF for enhanced seawater oxidation electrocatalysis

Weidong He, Zhicheng Yuan, Pengzhe Zhao, Ruiyu Pan, Junhao Zhang*, Qianqian Fan, Zhongyao Duan, Xiangjun Zheng, Fu Cao*, Xingmei Guo*

School of Environmental and Chemical Engineering, Jiangsu University of Science and Technology, Zhenjiang 212003, China.

**Corresponding authors: jhzhang6@just.edu.cn (J. Zhang), huanjing2001@163.com (F. Cao), guoxm@just.edu.cn (X. Guo)*

Experimental Section

Chemicals and Reagents

Cobalt nitrate hexahydrate ($Co(NO_3)_2 \cdot 6H_2O$), potassium hydroxide (KOH), anhydrous ethanol (C_2H_5OH), acetone (C_3H_6O), and ammonia solution ($NH_3 \cdot H_2O$) were purchased from China National Pharmaceutical Group Co., Ltd. Graphene oxide (GO) was procured from Xianfeng Nanomaterials Technology Co., Ltd. Titanium foam (TF) was supplied by Kunshan Shangte New Materials Co., Ltd. All reagents were analytical grade and required no further purification, with deionized water being used throughout the experimental process.

Catalyst Preparation

Preparation of $Co_xTi_4O_9$/TF. Titanium foam (TF) was firstly ultrasonically cleaned in acetone and ethanol sequentially for 15 min to remove surface oxides and impurities. After that, the pretreated TF was immersed in a 20 mL solution of 10 mol L^{-1} KOH at 90 ℃ for 6 h, followed by rinsing with deionized water and dried at 60 ℃ overnight to obtain the $K_2Ti_4O_9$ nanowire network precursor on TF. Then, the $K_2Ti_4O_9$/TF was subjected to ion exchange by immersing in 1 mol L^{-1} $Co(NO_3)_2 \cdot 6H_2O$ solution at 80 ℃ for 12 h, followed by rinsing with deionized water and vacuum drying overnight to obtain $Co_xTi_4O_9$/TF.

Preparation of $Co_3O_4/Co_xTi_4O_9$/TF. Typically, 0.3 g of $Co(NO_3)_2 \cdot 6H_2O$ was dispersed in a mixed solution of 15 mL ethanol and 15 mL deionized water. Under continuous stirring, 5 mL of ammonia was slowly added to the solution. After constant stirring for 1 h, the solution was transferred to a 70 mL polytetrafluoroethylene-lined stainless-steel autoclave. Meanwhile, the $Co_xTi_4O_9$/TF was placed in the autoclave liner and hydrothermally reacted at 80 °C for 10 h to grow Co_3O_4. A series of $Co_3O_4/Co_xTi_4O_9$/TF samples with different Co_3O_4 loadings were synthesized by adjusting the mass of $Co(NO_3)_2 \cdot 6H_2O$, denoted as x-$Co_3O_4/Co_xTi_4O_9$/TF (where x refers to the mass of $Co(NO_3)_2 \cdot 6H_2O$, x = 0.1, 0.2, 0.3, 0.4, 0.5 g). Unless otherwise stated, all $Co_3O_4/Co_xTi_4O_9$/TF samples mentioned in this work correspond to 0.3-$Co_3O_4/Co_xTi_4O_9$/TF.

Preparation of GO/Co_3O_4/$Co_xTi_4O_9$/TF. GO was loaded on the surface via electrodeposition, which was performed in a three-electrode system with Co_3O_4/$Co_xTi_4O_9$/TF served as the working electrode, Ag/AgCl as the reference electrode, and a carbon rod as the counter electrode. An aqueous dispersion of GO (0.5 mg mL^{-1}) was applied as electrolyte, and the electrodeposition was conducted at a potential of -1.1 V vs. Ag/AgCl. To optimize the loading amount of GO overlayer, different disposition duration was performed to obtain a series of y-GO/Co_3O_4/$Co_xTi_4O_9$/TF (where y denotes the electrodeposition time, y = 0, 40, 80, 120, 160 s). Unless otherwise stated, all references to GO/Co_3O_4/$Co_xTi_4O_9$/TF in this work correspond to 80-GO/Co_3O_4/$Co_xTi_4O_9$/TF.

Materials Characterization

The morphology and microstructure were examined using a field emission scanning electron microscope (FESEM, Merlin Compact model, Carl Zeiss GmbH, Germany) and a transmission electron microscope (TEM, JEM-2100F, Philips Netherlands). Elemental distribution was characterized by the accessory of energy dispersive spectrometer (EDS). Phase composition and surface elemental bonding states were analyzed using a X-ray diffraction instrument (XRD, XRD-6000 X model, Shimadzu Corporation) and X-ray photoelectron spectrometer (XPS, AXIS UltraDLD model, Shimadzu Corporation).

Electrochemical Testing

Electrocatalytic performances were tested using a three-electrode system on an electrochemical workstation (CHI660D), employing the as-prepared sample, Hg/HgO electrode and graphite rod as working, reference and counter electrodes, respectively. 1 mol L^{-1} KOH aqueous or seawater solutions were used as electrolytes. Seawater is naturally collected from the Bohai Bay. During testing, all measured voltages were converted to reversible hydrogen electrode potential (RHE) through the Nernst equation: $E_{(vs.\ RHE)} = E_{(vs.\ Hg/HgO)} + 0.059 \times pH + 0.098$. Linear sweep voltammetry (LSV) was performed at a scanning rate of 5 mV s^{-1} with 80% iR compensation. The Tafel slopes were calculated based on LSV plots using the formula $\eta = b \log | j | + a$ (where η represents the absolute value of the overpotential, j denotes current density,

and b is the Tafel slope). To evaluate charge transfer resistance during catalytic processes, electrochemical impedance spectroscopy (EIS) was conducted at 0.602 V vs. Hg/HgO with an amplitude of 5 mV and a frequency range from 100 kHz to 0.01 Hz. For estimating the electrochemical active surface area (ECSA) through double layer capacitance (C_{dl}), cyclic voltammetry (CV) curves were recorded between 0.1 - 0.2 V vs. Hg/HgO with different sweeping rates. Catalytic stability was assessed through a chronoamperometric test performed at 0.602 V vs. Hg/HgO.

Supplementary Figures

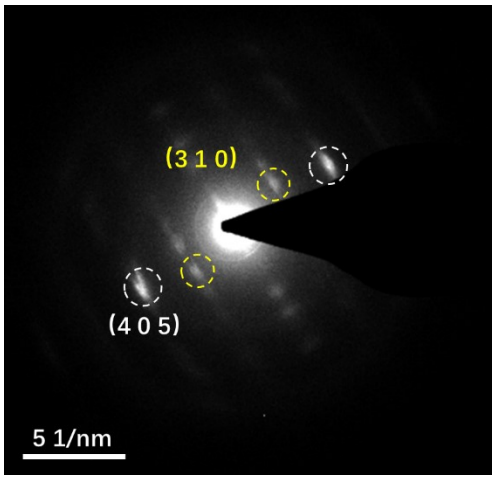

Fig. S1 SAED pattern of the $Co_xTi_4O_9$ region.
Note: The selected area electron diffraction (SAED) pattern identified the (310) and (405) planes of $Co_xTi_4O_9$. The diffraction spot of the (200) plane was obscured by the brightness of the central spot.

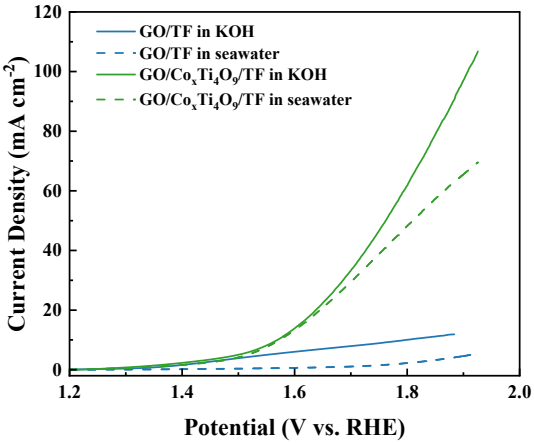

Fig. S2 LSV curves of GO/TF and GO/$Co_xTi_4O_9$/TF in KOH and alkaline seawater.
Note: The GO/$Co_xTi_4O_9$/TF electrode in alkaline seawater exhibits comparable performance with that in aqueous electrolyte, especially at potentials below 1.7 V vs. RHE, demonstrating that the synergy between GO and $Co_xTi_4O_9$ can enhance the stability in seawater.

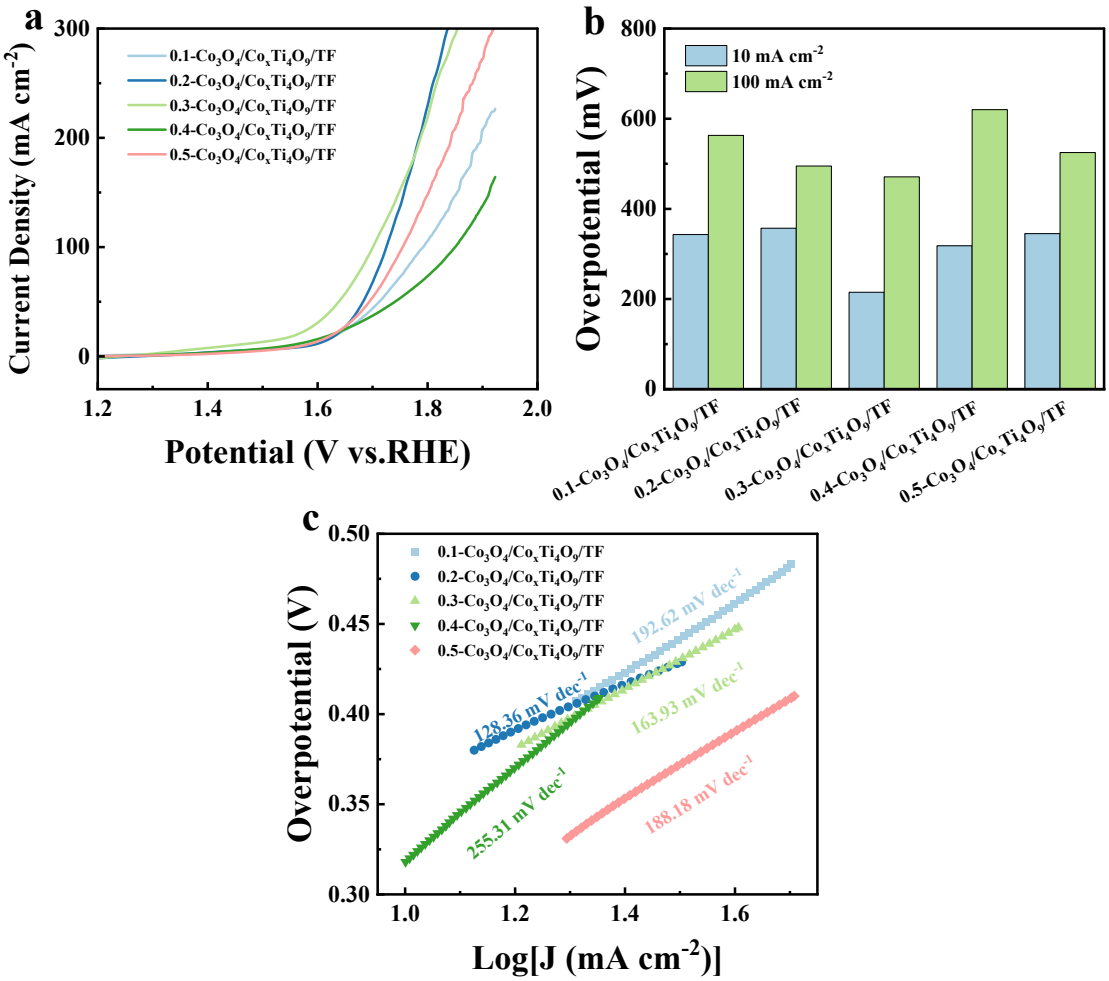

Fig. S3 (a) LSV curves of $Co_3O_4/Co_xTi_4O_9$/TF with different Co_3O_4 loading amounts in 1 mol L^{-1} KOH (x-$Co_3O_4/Co_xTi_4O_9$/TF, where x=0.1~0.5 referring to the 0.1~0.5 g of $Co(NO_3)_2 \cdot 6H_2O$ precursor in the preparation process); (b) Overpotentials at current densities of 10 mA cm^{-2} and 100 mA cm^{-2} ; (c) Tafel slopes.

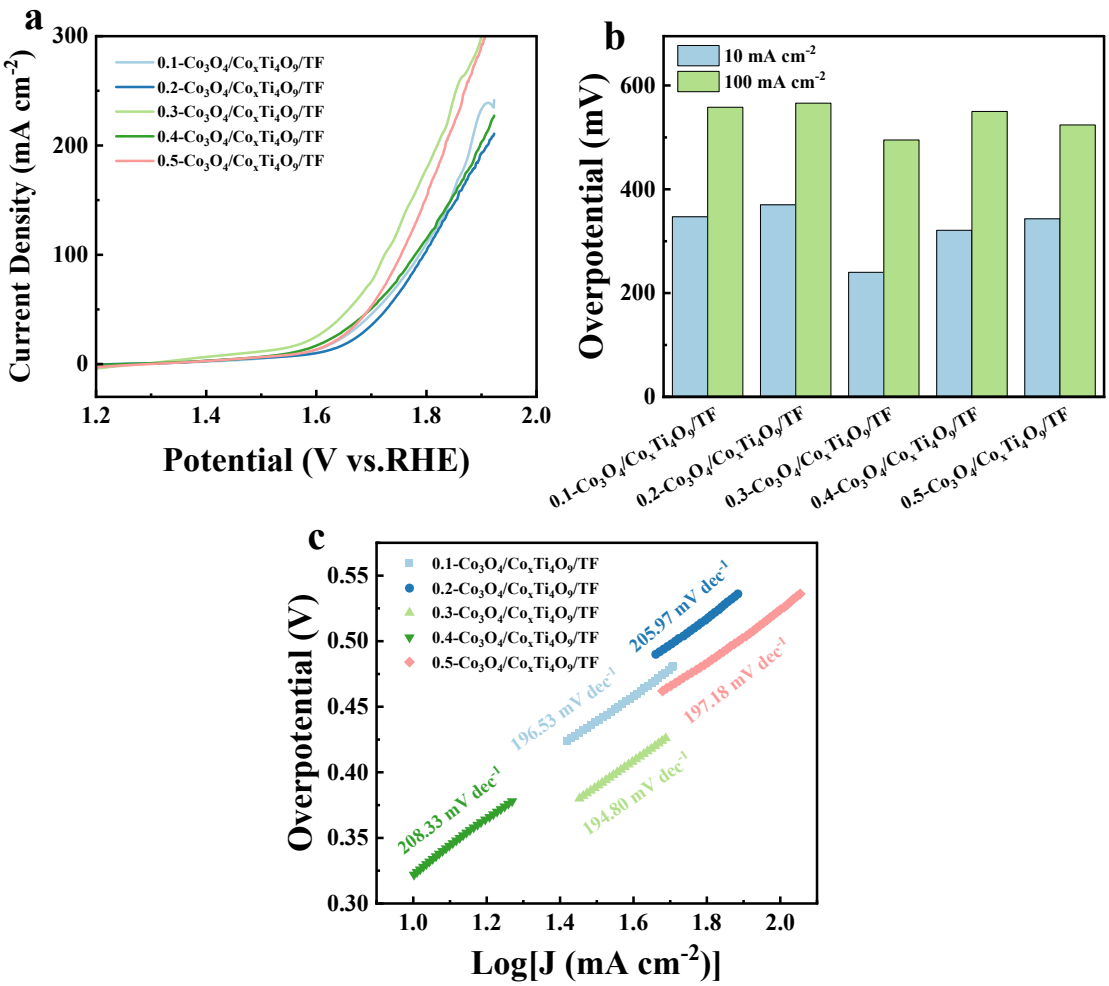

Fig. S4 (a) LSV curves of $Co_3O_4/Co_xTi_4O_9$/TF with different Co_3O_4 loading amounts in alkaline seawater (x-$Co_3O_4/Co_xTi_4O_9$/TF, where x=0.1~0.5 referring to the 0.1~0.5 g of $Co(NO_3)_2 \cdot 6H_2O$ precursor in the preparation process); (b) Overpotentials at current densities of 10 mA cm^{-2} and 100 mA cm^{-2} ; (c) Tafel slopes.

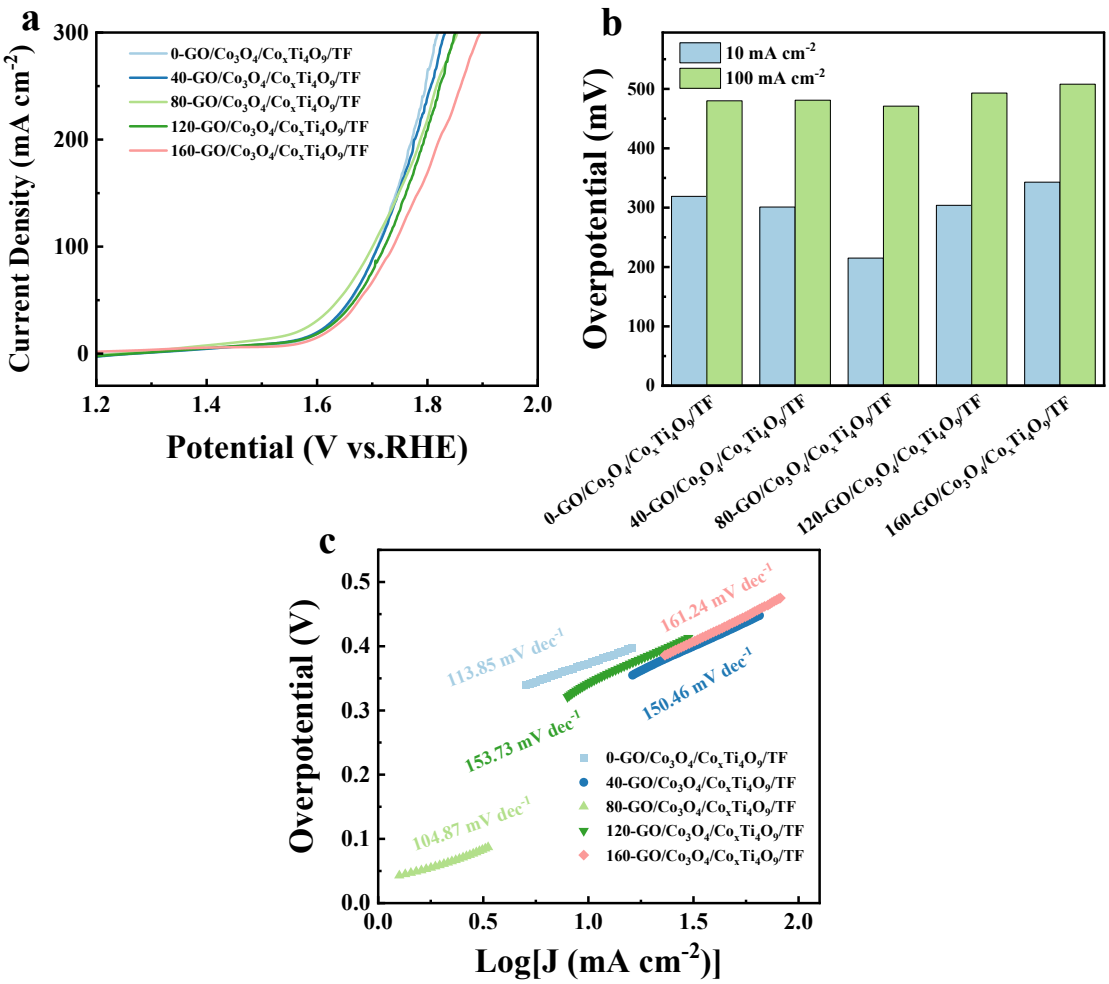

Fig. S5 (a) LSV curves of GO/Co_3O_4/$Co_xTi_4O_9$/TF with different GO loading amounts in 1 mol L^{-1} KOH (y-GO/Co_3O_4/$Co_xTi_4O_9$/TF, where y=0~160 referring to the 0~160 s of the electrodeposition time for GO); (b) Overpotentials at current densities of 10 mA cm^{-2} and 100 mA cm^{-2} ; (c) Tafel slopes.

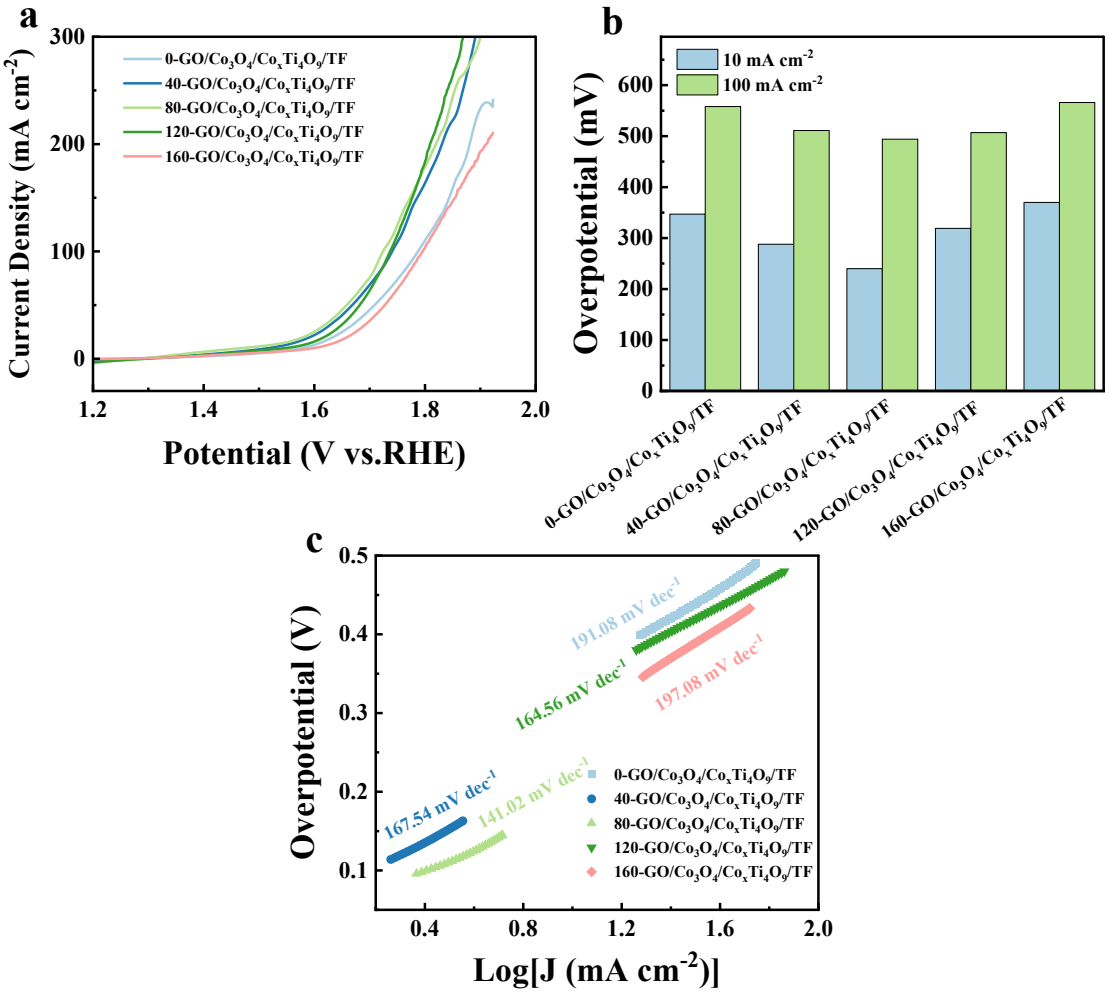

Fig. S6 (a) LSV curves of $GO/Co_3O_4/Co_xTi_4O_9/TF$ with different GO loading amounts in alkaline seawater (y-$GO/Co_3O_4/Co_xTi_4O_9/TF$, where y=0~160 referring to the 0~160 s of the electrodeposition time for GO); (b) Overpotentials at current densities of 10 mA cm^{-2} and 100 mA cm^{-2} ; (c) Tafel slopes.

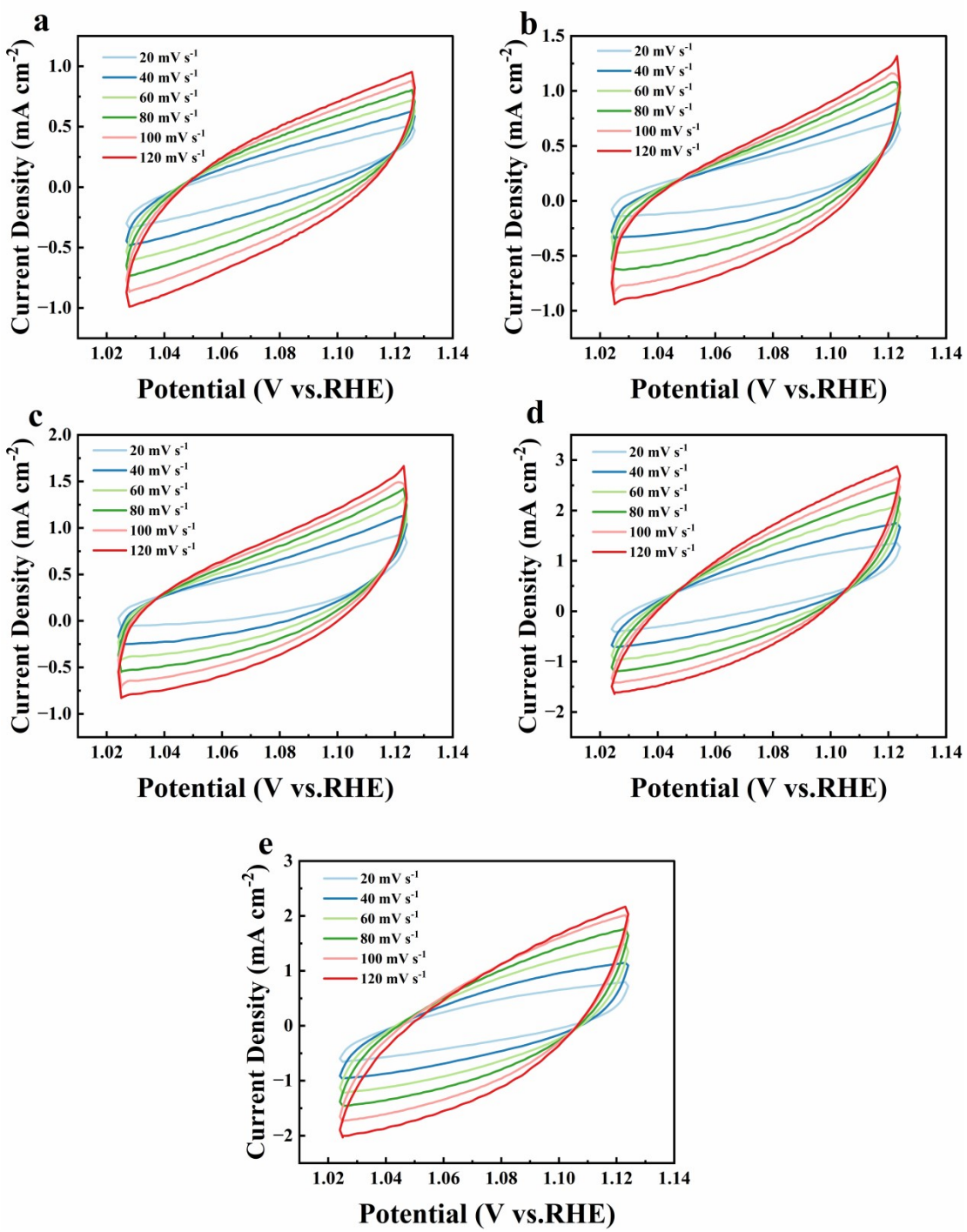

Fig. S7 CV curves of different samples in the non-Faradaic potential range with scan rate increasing from 20 to 120 mV s^{-1}. (a) $Co_xTi_4O_9$/TF in 1 mol L^{-1} KOH; (b) $Co_3O_4/Co_xTi_4O_9$/TF in 1 mol L^{-1} KOH; (c) $Co_3O_4/Co_xTi_4O_9$/TF in alkaline seawater; (d) GO/$Co_3O_4/Co_xTi_4O_9$/TF in 1 mol L^{-1} KOH; (e) GO/$Co_3O_4/Co_xTi_4O_9$/TF in alkaline seawater.

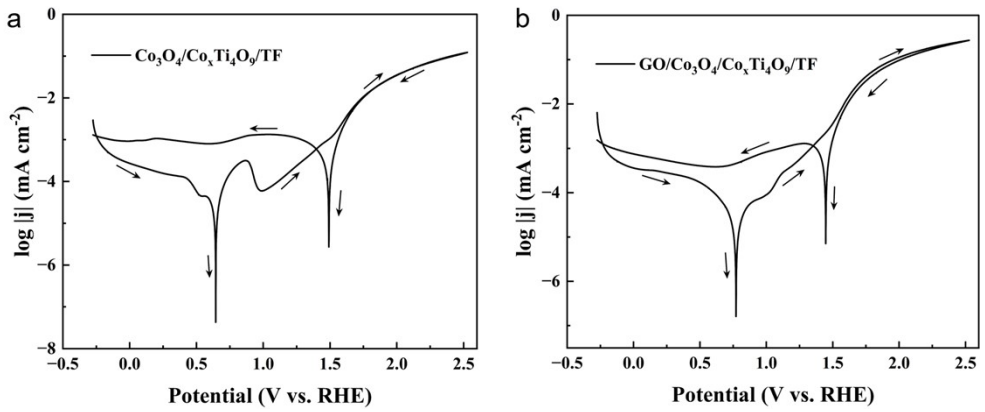

Fig. S8 Cyclic potentiodynamic polarization curves of $Co_3O_4/Co_xTi_4O_9$/TF (a) and $GO/Co_3O_4/Co_xTi_4O_9$/TF (b) in alkaline seawater.

Supplementary Tables

Table S1 Percentage of each bonding state estimated from deconvolution area of high-resolution Co 2p spectrum.

Sample	Satellite %	Co $2p_{1/2}$ (%)		Satellite %	Co $2p_{3/2}$ (%)	
		Co^{3+}	Co^{2+}		Co^{3+}	Co^{2+}
GO/Co_3O_4/ $Co_xTi_4O_9$/TF	25.32	42.75	31.93	22.11	44.43	33.46

Note: Based on the deconvoluted peak area, the Co^{2+}/Co^{3+} ratio in GO/Co_3O_4/$Co_xTi_4O_9$/TF is determined to be around 3:4. In contrast, stoichiometric Co_3O_4 has a well-defined Co^{2+}/Co^{3+} ratio of 1:2. The higher ratio detected by XPS is attributed to the additional Co^{2+} signal contributed by $Co_xTi_4O_9$.

Table S2 Comparison of the OER catalytic activity of GO/Co_3O_4/$Co_xTi_4O_9$/TF with other reported high-performance Co-based OER catalysts.

Electrocatalysts	Electrolyte	Current Density (mA cm^{-2})	Overpotential (mV)	Ref
GO/Co_3O_4/$Co_xTi_4O_9$/TF	**Alkaline seawater**	**10**	**240**	**This work**
NZ700/GF	Alkaline seawater	10	281	[S1]
Co-$NiFeO_x$/NIF	Alkaline seawater	10	240	[S2]
ER-SNCF-20s	Alkaline seawater	10	278	[S3]
CeO_2/CoNiP@NF	Alkaline seawater	10	249	[S4]
NiRu-LDH@pWD	Alkaline seawater	10	260	[S5]
NiCoS/NF	Alkaline seawater	10	280	[S6]
CoSe/$MoSe_2$	Alkaline seawater	10	540	[S7]
Co_3FePM-TPDA	Alkaline seawater	10	331	[S8]
Ni-Co-MoS_2	1 mol L^{-1} KOH	10	227	[S9]
Co-EA	1 mol L^{-1} KOH	10	268	[S10]
300-h/Co/CC	1 mol L^{-1} KOH	10	280	[S11]

Table S3 The fitting data of Nyquist plots obtained in 1 mol L^{-1} KOH and alkaline seawater.

Samples	R_s (Ω)	R_{ct} (Ω)
$Co_xTi_4O_9$/TF in KOH	3.664	106.7
$Co_3O_4/Co_xTi_4O_9$/TF in KOH	3.795	51.8
GO/$Co_3O_4/Co_xTi_4O_9$/TF in KOH	3.56	39.5
$Co_3O_4/Co_xTi_4O_9$/TF in seawater	3.289	88.8
GO/$Co_3O_4/Co_xTi_4O_9$/TF in seawater	2.893	53.7

References

[S1] T.K. Sana Fathima, A. Ghosh, S. Ramaprabhu. Efficient, chlorine-free, and durable alkaline seawater electrolysis enabled by MOF-derived nanocatalysts. *Int. J. Hydrogen Energy.,* 2024, 90, 546-556.

[S2] H. L. Zhao, S. L. Liu, F. Y. Tian, H. D. Li, L. T. Xin, W. P. Xiao, G. R. Xu, D. H. Chen, T. Y. Ma, E. Egamberdiev, S. Donaev, Y. X. Zong, G. Y. Fu, Z. X. Wu, L. Wang. Trace cobalt accelerates the structural reconstruction to generate high-valence nickel for water-splitting in seawater media. *Chem. Eng. J.,* 2025, 515, 163388.

[S3] R. G. Hu, M. Y. Zhao, H. Miao, F. Y. Liu, J. Q. Zou, C. F. Zhang, Q. Wang, Z. Q. Tian, Q. J. Zhang, J. L. Yuan. Rapidly reconstructing the active surface of cobalt-based perovskites for alkaline seawater splitting. *Nanoscale*, 2022,14, 10118-10124

[S4] X. L. Yang, C. Z. Li, H. Y. Song, Y. N. Kou, Q. Wu, G. Zhao, C. Y. Wu, J. P. Ma, L. L. Bo, J. H. Tong. CeO_2/CoNiP heterojunction as excellent OER electrocatalysts in alkaline seawater effectively suppresses chloride corrosion and cobalt leaching. *ACS Sustainable Chem. Eng.,* 2025 13 (33), 13561-13572.

[S5] Q. L. Zhou, N. Li, J. J. Liu, G. Y. Chen, X. Qin, Z. C. Wang, Y. F. Wei, Z. Liu. Electronic structure engineering of Ru-doped Ni-based-LDH toward high-performance seawater electrolysis. *Carbon*, 2026, 254, 121530.

[S6] C. Z. Wang, M. Z. Zhu, Z. Y. Cao, P. Zhu, Y. Q. Cao, X. Y. Xu, C. X. Xu, Z. Y. Yin. Heterogeneous bimetallic sulfides based seawater electrolysis towards stable industrial-level large current density. *App. Catal. B: Environ.*, 2021, 291, 120071.

[S7] J. P. Sun, J. Li, Z. Z. Li, C. H. Li, G. M. Ren, Z. S. Zhang, X. C. Meng. Modulating the electronic structure on cobalt sites by compatible heterojunction fabrication for greatly improved overall water/seawater electrolysis. *ACS Sustainable Chem. Eng.*, 2022, 10 (30), 9980-9990.

[S8] Y. W. Dong, M. Y. Wu, Y. Ren, Z. Yu, Z. Zhao. Big pyridyl Schiff base π-conjugated skeleton based cobalt/iron metal complexes: bimetallic electrocatalysts for the oxygen evolution reaction. *J. Mater. Chem. C*, 2025,13, 4170-4179.

[S9] W. Jiang, J. J. Li, C. X. Zhao, W. W. Cheng, J. L. Liu, Y. L. Chen. OER performance of water electrolysis by micron MoS_2 enhanced nickel-cobalt composite

electrode. *Int. J. Hydrogen Energy.*, 2024, 51: 1486-1496.

[S10] R. Tu, W. Song, J. W. Liu, C. T. F. Zhang, Q. Z. Li, S. Zhang, T. Goto. Mist-CVD: A novel route to high-performance OER catalysts of Co- and Ni-based hollow microspheres. *J. Alloy. Compd.,* 2025, 1046: 184853.

[S11] T. Kang, J. Kim. Optimal cobalt-based catalyst containing high-ratio of oxygen vacancy synthesized from metal-organic-framework (MOF) for oxygen evolution reaction (OER) enhancement. *Appl. Surf. Sci.*, 2021, 560: 150035.